



UPPSALA
UNIVERSITET

Uppsala University

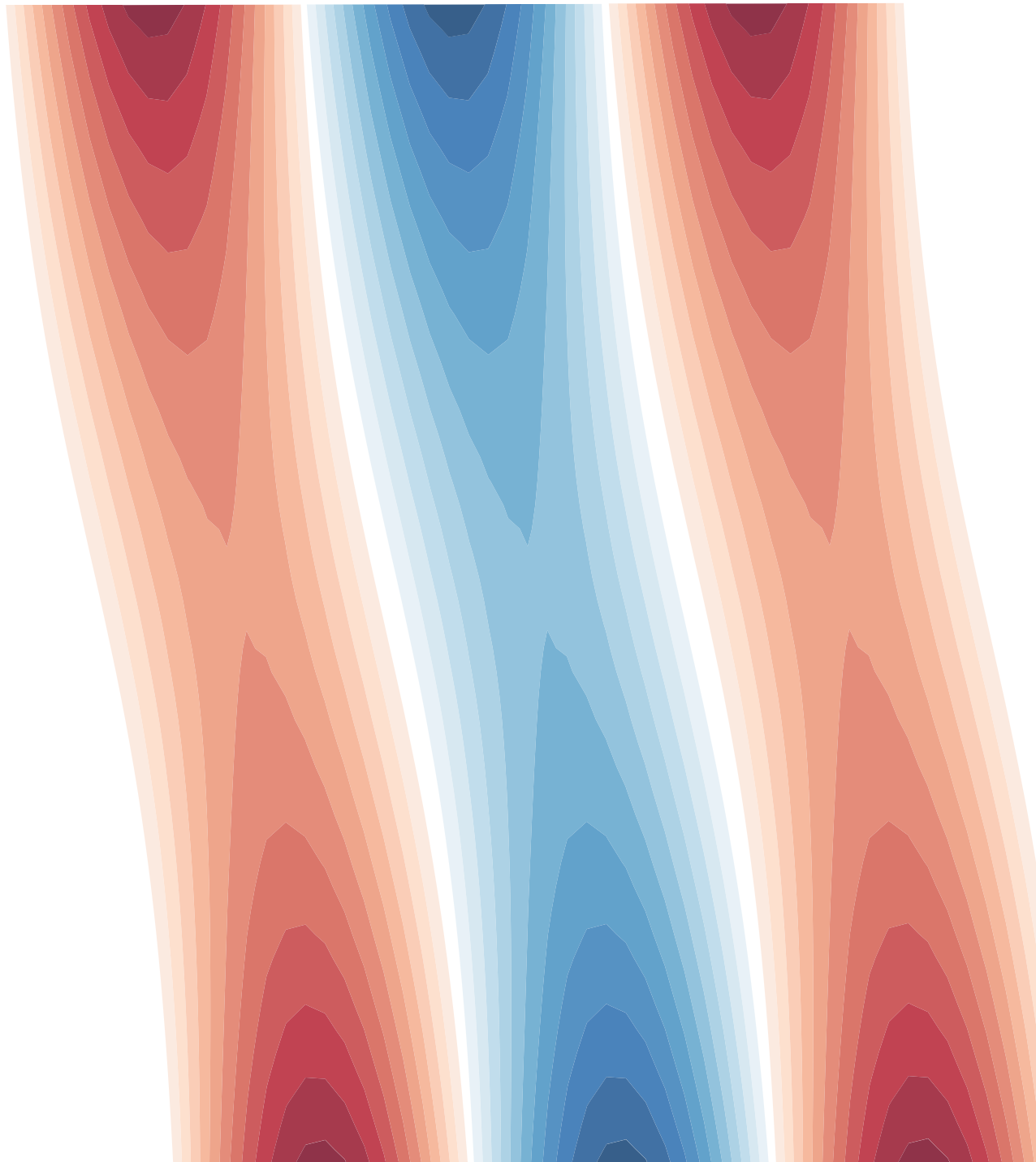
Project in Meteorology

January, 2025

Revisiting the Eady Problem using a Pseudospectral approach

Juan Vázquez Portillo

Supervisor: Antonio Segalini





UPPSALA
UNIVERSITET

Abstract

This study revisits the Eady problem using a pseudospectral numerical approach, known for its simple analysis of baroclinic instability in a stratified fluid. The Eady model is explored in linear and nonlinear regimes, where the growth rates, perturbation dynamics and the interaction with the background zonal flow have been analyzed. The study validates the model by comparing the analytical growth rate of the Eady problem with the numerical simulations, ensuring the accuracy of the used pseudospectral method. This study examines how the growing of the baroclinic instability can be influenced through the variation of different parameters, such as, the initial perturbations, the Coriolis parameters (f_0 and β), and velocity profiles. Furthermore, a realistic scenario is studied using ERA5 reanalysis data to simulate atmospheric conditions, where the density is implemented with a height dependency. This revealed how the background zonal wind can affect the formation and evolution of Rossby waves and baroclinic instability. The results can be used as a foundation to explore more complex processes such as the dynamics of cyclogenesis and blocking events.

1 Introduction

Baroclinic instability is an important mechanism which drives the large-scale dynamics that take place in the atmosphere and oceans (Pierrehumbert and Swanson, 1995). It leads to the growth of disturbances through the interaction of stratification, planetary rotation and vertical shear. This project focuses on the Eady model, a foundational framework for understanding how baroclinic instability emerges.

The Eady model, proposed by Eric Eady, is one of the first mathematical approaches to baroclinic instability (Eady, 1949). This model simplifies the atmosphere assuming two rigid lids: the lower and the upper lid correspond to the Earth boundary layer and the tropopause, respectively. This simplified model, which has an analytic solution, provides an analytical and computational framework to explore the growth and evolution of disturbances under idealized conditions.

This study investigates several aspects of the Eady model. Firstly, the growth rate derived from the analytical solution is compared with the computational results to ensure consistency. Once the model is validated, different parameters are modified and added to explore their impact on wave growth rates and maximum meridional velocities, for the linear and nonlinear Eady problem. Two initial perturbations are tested to understand how different excitation mechanisms influence the instability's evolution. One focuses on a specific wavenumber and another which excites all the wavenumbers. Finally, the vertical velocity profile is generalized incorporating a polynomial shear profile and studying a realistic application using the ERA5 reanalysis data.

This project intends to expand the knowledge of the Eady model and how diverse parameters affects the growth of the baroclinic instability using numerical simulations based on pseudospectral methods.

2 Background

The Eady Model

In the Eady model, the fluid trapped between these two lids follows the quasi-geostrophic approximation and a f -plane motion (i.e. constant Coriolis parameter). The density, ρ , and the Brunt–Väisälä frequency, N , are assumed to be constant, giving an incompressible and uniformly stratified fluid. The model proposed by Vallis will be used as a reference framework, where a streamfunction, Ψ and a basic state of potential vorticity, Q , are assumed (Vallis, 2017). The Eady model analytical solution will be used to validate the present model. The background state in the canonical Eady problem is given by

$$\Psi = U_{\max} \frac{z}{H} y = U_0 y, \quad (1)$$

where U_{\max} is the maximum zonal wind, z and y are the height and latitudinal coordinates, respectively, and H is the height of the vertical layer. The streamfunction indicates a basic state with uniform vertical shear, which only depends on the vertical coordinate z .

Spontaneous baroclinic instability in the Eady model can be seen as two boundary Rossby waves interacting and enhancing (Hoskins et al., 1985). Figure 1 shows a scheme of these processes, where the induced clockwise circulation in the top, Fig-

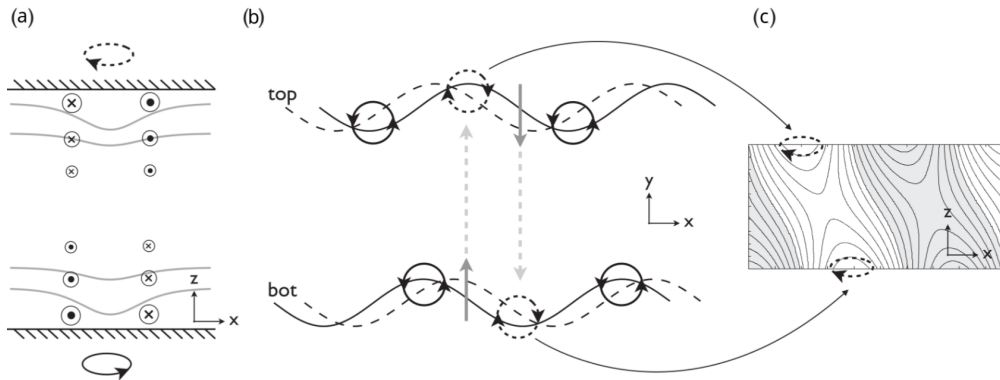


Figure 1: Schema of how Rossby waves interact in the Eady model, generating baroclinic instability. **a)** shows the circulation generated due to the thermal wind. **b)** x - y view of the generated shift. This phase shift appears in **c)**, where the Eady wave pattern appears in the x - z plane. Figure from Shih-Nan et al., 2020

ure 1b), generates a shift which evolves in an upwind propagation of the waves. An opposite behaviour takes place for the bottom wave. The growth of both waves occurs when there is a $\pi/2$ phase shift, namely when they are in quadrature. The growth of the disturbance in this baroclinic instability process is due to a wave phase locking (Shih-Nan et al., 2020). Eady growth rate and wavelength for the most unstable waves are given by

$$\sigma_E = 0.31 f_0 R_i^{-2} \quad , \quad \lambda_E \approx 3.9 L_d \quad , \quad (2)$$

where the Richardson number and the deformation radius are defined as

$$R_i = \frac{N^2}{(U/H)^2} \quad , \quad L_d = \frac{NH}{f_0} \quad . \quad (3)$$

3 Methodology

The equations used for solving the Eady problem are expressed in potential vorticity formulation, where the potential vorticity conservation is given by

$$\frac{Dq}{Dt} = \frac{\partial q}{\partial t} + u \frac{\partial q}{\partial x} + v \frac{\partial q}{\partial y} + w \frac{\partial q}{\partial z} = 0 \quad (4)$$

with the potential vorticity computed as

$$q = \nabla_h^2 \psi + f + \frac{f_0^2}{\rho} \frac{\partial}{\partial z} \left(\frac{\rho}{N^2} \frac{\partial \psi}{\partial z} \right). \quad (5)$$

The initial ψ is defined as (1), reaching a maximum at the top vertical layer. The Coriolis parameter is moved to the left-hand side, resulting in

$$\frac{D(q - f)}{Dt} = -v\beta, \quad (6)$$

where $\beta = \frac{\partial f}{\partial y}$ is the Coriolis parameter variation with the latitude and u and v are the zonal and meridional velocity components, respectively. The quasigeostrophic system must be closed by relating the flow field (u, v) to the vorticity (q) using the streamfunction-potential vorticity relation defined as

$$u = -\frac{\partial \psi}{\partial y}, \quad v = \frac{\partial \psi}{\partial x} \quad (7)$$

As stated before, the Eady model is usually implemented in a context where two rigid boundary conditions are found in the height coordinate, representing the boundary layer and the tropopause. Boundary conditions are assumed periodic in x and y and Neumann type in z , which are defined as

$$\left. \frac{D}{Dt} \frac{\partial \psi}{\partial z} \right|_{bottom} = 0, \quad \left. \frac{D}{Dt} \frac{\partial \psi}{\partial z} \right|_{top} = 0 \quad (8)$$

Due to the implementation of periodic problems, the straightforward handling of the linear terms, the efficient computation, and higher accuracy even for low resolution, the Fourier Spectral Method is used to solve the equations in the x - y direction. Thus, the

model is assumed to be a "z-layer model", where a finite differences scheme is used in the z direction. The potential vorticity equation (5) in Fourier space is given by

$$\hat{q} = -(k_x^2 + k_y^2)\hat{\psi} + \hat{f} + \frac{f_0^2}{N^2} \frac{\partial^2 \hat{\psi}}{\partial z^2}, \quad (9)$$

where buoyancy and density are assumed constant with height and the hat notation indicates the variables in spectral space. Note that the laplacian operator becomes $-(k_x^2 + k_y^2)$ in spectral space. For handling the nonperiodic boundary conditions in z , second-order finite difference discretization is implemented for the last term in (9), where a central scheme is chosen with an uniform grid,

$$\frac{f_0^2}{N^2} \frac{\partial^2 \hat{\psi}}{\partial z^2} \approx \frac{f_0^2}{N^2} \frac{\hat{\psi}_{i+1} - 2\hat{\psi}_i + \hat{\psi}_{i-1}}{\Delta z^2}. \quad (10)$$

For the boundary conditions, first-order schemes are used for the top and bottom layers, respectively, as

$$\left. \frac{\partial \hat{\psi}}{\partial z} \right|_{top} \approx \frac{\hat{\psi}_i - \hat{\psi}_{i-1}}{\Delta z}, \quad \left. \frac{\partial \hat{\psi}}{\partial z} \right|_{bottom} \approx \frac{\hat{\psi}_{i+1} - \hat{\psi}_i}{\Delta z}. \quad (11)$$

This allows a more efficient and cost-effective resolution of the equations, as will be shown below. The methodology for simulating the Eady problem starts with an initial value of $\hat{\psi}$. With this initial condition, the next time step of the potential vorticity is obtained using (6). Once this new potential vorticity value is obtained, (9) has to be inverted to get the streamfunction for the next time step. The inversion problem is given by $\mathbf{D}\hat{\psi} = \mathbf{B}$, where

$$\mathbf{D} = \begin{bmatrix} d_{00} & d_{01} & & & \\ d_{10} & d_{11} & d_{12} & & \\ & \ddots & \ddots & \ddots & \\ & & d_{10} & d_{11} & d_{12} \\ & & & d_{00} & d_{01} \end{bmatrix} \quad (12)$$

with

$$d_{00} = -\frac{1}{\Delta z} = -d_{01},$$

$$d_{10} = \frac{f_0^2}{N^2} \frac{1}{\Delta z^2} = d_{12},$$

$$d_{11} = -(k_x^2 + k_y^2) - 2 \frac{f_0^2}{N^2} \frac{1}{\Delta z^2},$$

and

$$\mathbf{B} = \left[\left. \frac{\partial \hat{\psi}}{\partial z} \right|_{bottom}, \hat{q}, \left. \frac{\partial \hat{\psi}}{\partial z} \right|_{top} \right]^T, \quad (13)$$

where a band solver is used to improve the computational cost. It is worth noting that the use of a first-order finite difference method for the boundary conditions implies a significant advantage in computational cost due to the tridiagonal structure of (12). In contrast, a penta-diagonal structure would arise if a higher-order scheme as in the inner domain is used. Once the streamfunction at the next time step can be solved, the associate velocities

$$\hat{v} = ik_x \hat{\psi}, \quad \hat{u} = -ik_y \hat{\psi}, \quad (14)$$

can be computed. Finally (6) can be solved, thus obtaining the potential vorticity value and continuing with the inversion problem for the following time step. This time variation problem,

$$\frac{D(q-f)}{Dt} = \frac{Dq}{Dt} - \frac{Df}{Dt} = \frac{\partial q}{\partial t} + u \frac{\partial q}{\partial x} + v \frac{\partial q}{\partial y} - v\beta, \quad (15)$$

have different nonlinear terms. In this project, both nonlinear and linear approaches are explored for solving the Eady problem, demonstrating the extent to which one can advance within the framework of the hydrostatic quasi-geostrophic approximation. Some authors have already discussed the limits of these approximations (Garner et al., 1992), where one key aspect in frontal development is the advection of relative vorticity by the cross-frontal circulation. This is ignored in quasigeostrophic approximations.

To accomplish that, potential vorticity and the velocities can be split into basic states and perturbations as

$$q = q_0 + q', \quad u = u_0 + u', \quad v = v_0 + v', \quad (16)$$

where the subscript 0 denotes the mean flow, while the prime represents the variations. The mean velocity field in the y -direction is 0. This decomposition is introduced to address the periodicity problem, where the flow is separated into a steady background state and its variations. It is further assumed that this background flow remains unmodified and is not influenced by the perturbations. However, this assumption is not realistic and will lead into an exponential growth of the perturbation due to the continuous feedback driven by baroclinic instability, regardless of whether a linear or nonlinear model is used. To properly account for the interaction between perturbations and the mean flow, it would be necessary to eliminate periodicity in at least one coordinate, such as the y -coordinate. To determine the value of q , (1) can be substituted into (5), resulting in $q_0 = 0$, leaving only the potential vorticity perturbation. By adding this decomposition to (15), one obtains

$$\frac{\partial q}{\partial t} = - \underbrace{\left(u_0 \frac{\partial q'}{\partial x} + v' \beta \right)}_{\text{LINEAR TERM}} - \underbrace{\left(u' \frac{\partial q'}{\partial x} + v' \frac{\partial q'}{\partial y} \right)}_{\text{NONLINEAR TERM}}, \quad (17)$$

where the potential vorticity time variation is split into linear and nonlinear contributions, respectively, and $\beta = \frac{\partial q_0}{\partial y}$, after substituting (16) into (5). This equation can be expressed in the spectral space as

$$\frac{\partial \hat{q}}{\partial t} = - (u_0 i k_x \hat{q} + \beta \hat{v}') - (i k_x \hat{u}' \hat{q} + i k_y \hat{v}' \hat{q}), \quad (18)$$

where the nonlinear terms, $\hat{u}' \hat{q}$ and $\hat{v}' \hat{q}$, are handled using a pseudo-spectral approach (Mendes et al., 2019). This method involves transforming to physical space to compute the multiplications and then returning to spectral space to proceed with the remaining calculations. A Leap-frog scheme is adopted to update the potential vorticity and the boundary conditions (Iserles, 1986). This method has a good balance between efficiency and accuracy, offering more stability than the Euler method for larger time steps. The first time step, which serves as the starting point for the Leap-frog scheme, is obtained using an explicit Euler scheme.

Boundary conditions

The same approach can be followed with the boundary conditions to obtain their value at the next time step. The stream function can be split into a mean state and a perturbative contribution as $\psi = \psi_0 + \psi'$.

Using (8) and applying the same decomposition as in (17), the time evolution of the vertical derivative of the streamfunction in the spectral space can be expressed as

$$\frac{\partial}{\partial t} \left(\frac{\partial \hat{\psi}'}{\partial z} \right) = - \underbrace{\left(u_0 i k_x \frac{\partial \hat{\psi}'}{\partial z} - \hat{v}' u_0 z \right)}_{\text{LINEAR TERM}} - \underbrace{\left(i k_x \hat{u}' \frac{\partial \hat{\psi}'}{\partial z} + i k_y \hat{v}' \frac{\partial \hat{\psi}'}{\partial z} \right)}_{\text{NONLINEAR TERM}}. \quad (19)$$

General velocity profile

The result obtained in (18) is only valid for a linear shear profile which only changes with height, where the streamfunction is defined as (1) having that $\partial^2 \psi / \partial z^2 = 0$ in (9). To extend the wind profile to any geometry (with dependency only on z), this second derivative has to be considered. This results in

$$\frac{\partial \hat{q}}{\partial t} = - \left(u_0 i k_x \hat{q} + \beta \hat{v}' - \hat{v}' \left(\frac{f_0}{N} \right)^2 \frac{\partial^2 \psi_0}{\partial z^2} \right) - (i k_x \hat{u}' \hat{q} + i k_y \hat{v}' \hat{q}). \quad (20)$$

For a more realistic scenario, density ρ should change with height. To implement this in the model, the definition of the Brunt–Väisälä frequency (Vallis, 2017)

$$N = \sqrt{-\frac{g}{\rho_0} \frac{\partial \rho(z)}{\partial z}} \quad (21)$$

is exploited substituting it into (5), obtaining that

$$q = \nabla_h^2 \psi + f + \frac{f_0^2}{N^2} \frac{\partial^2 \psi}{\partial z^2} - \frac{f_0^2}{g} \frac{\partial \psi}{\partial z}. \quad (22)$$

This new term is implemented in the model modifying d_{10} and d_{12} in (12) as

$$d_{10} = \frac{f_0^2}{N^2} \frac{1}{\Delta z^2} - \frac{f_0^2}{g} \frac{1}{2\Delta z}, \quad d_{12} = \frac{f_0^2}{N^2} \frac{1}{\Delta z^2} + \frac{f_0^2}{g} \frac{1}{2\Delta z}.$$

Aliasing

Due to the nature of spectral methods and the presence of nonlinear terms, aliasing arises because of the generation of frequencies beyond the Nyquist frequency (Lévesque, 2001). Aliasing can lead to high energy accumulation in lower wavenumbers, distorting the physical solution where baroclinic instability emerges. To mitigate these adverse effects, the 3/2 rule for dealising is applied in the transformations between real and spectral space where FFT algorithms are exploited (Bardos and Tadmor, 2013).

3.1 Numerical settings

The following constant parameter values are used in the presented model:

$L_x = 8000 \text{ km}$	$L_y = 8000 \text{ km}$	$H = 10 \text{ km}$
$N_x = 64$	$N_y = 16$	$N_z = 50$
$N = 0.01 \text{ s}^{-1}$	$f_0 = 0.0001 \text{ rad s}^{-1}$	$U_{\max} = 10 \text{ ms}^{-1}$
$dt = 3900 \text{ s}$	$E_r = 6371 \text{ km}$	$\Omega = 7.29 \cdot 10^{-5} \text{ s}^{-1}$

(23)

Once the vertical length is defined to match the troposphere height, the lengths for the horizontal direction can be derived using (2), where the constant parameters are previously substituted in (3). Thus, a horizontal length for the most unstable wavelength is obtained as

$$\lambda_E \approx 3.9L_d = \frac{L_x}{p}, \quad (24)$$

(Vallis, 2017), where p represents the wavenumber with the most unstable mode for the given domain length (i.e. to excite the second wavenumber, a domain of at least 7800 km would be required). A time step of 3900 seconds is chosen to ensure compliance with the Courant-Friedrichs-Lewy (CFL) condition, (Courant, 2018), as

$$CFL = u_{\max} \pi \frac{\Delta t}{\Delta x} = 0.98 < 1,$$

restricts the time step based on the maximum velocity in the domain, ensuring numerical stability. u_{\max} represents the maximum velocity in the domain, including contributions from both the background flow and any added perturbations.

Initialization

To have baroclinic instability, an initial perturbation must be added to the background flow (Kalashnik et al., 2022). For the sake of simplicity, this perturbation is added to q . Two different approaches are used to initialize a perturbation. A first scenario where a random initial perturbation affects only the boundaries (i.e. where the baroclinic instability is generated, Figure 1), and a second scenario, where a wavy initial perturbation excites only one wavenumber. This second approach will help to check how the different wavenumbers affect the baroclinic instability growth. A well-known analytical result for the linear case which serves as a model validation. In this second scenario, the following form of small perturbation

$$q = 0.001 \left[\cosh\left(\frac{\mu z}{L_z}\right) - \frac{U_{\max}}{\mu c} \sinh\left(\frac{\mu z}{L_z}\right) \cos(k_p x) \right], \quad (25)$$

(Vallis, 2017), is applied to the vorticity field. Where $\mu = L_d k_p$ and

$$c = \frac{U_{\max}}{2} + \frac{U_{\max}}{\mu} \sqrt{\left(\frac{\mu}{2} - \coth\frac{\mu}{2}\right) \left(\frac{\mu}{2} - \tanh\frac{\mu}{2}\right)}. \quad (26)$$

Different constant values for f_0 and β are also allowed in the simulation, where a latitude parameter φ is defined and

$$f_0 = 2\Omega \sin(\varphi) \quad , \quad \beta = \frac{2\Omega}{E_r} \cos(\varphi). \quad (27)$$

4 Results

Eady waves are the consequence of baroclinic instability, which grows over time. Thus, 20 days are chosen to run the different simulations, in conjunction with the parameters in (23).

Figure 2 illustrates a 3D representation of the Eady waves. Noticeably, the pattern is constant with height and longitude in the y - z and the x - y direction, respectively. Hence, there is no variation in the latitudinal axis. The Eady wave pattern is present in the x - z direction. As a result, many studies related to the Eady model focus exclusively on the x - z axis, using a 2D framework that reduces computational costs while achieving similar results (Mukougawa and Ikeda, 1994; Kalashnik and Chkhetiani, 2018; Williams, 1967). In this work, a 3D scenario is chosen to establish a foundation to explore the 3D wave evolution.

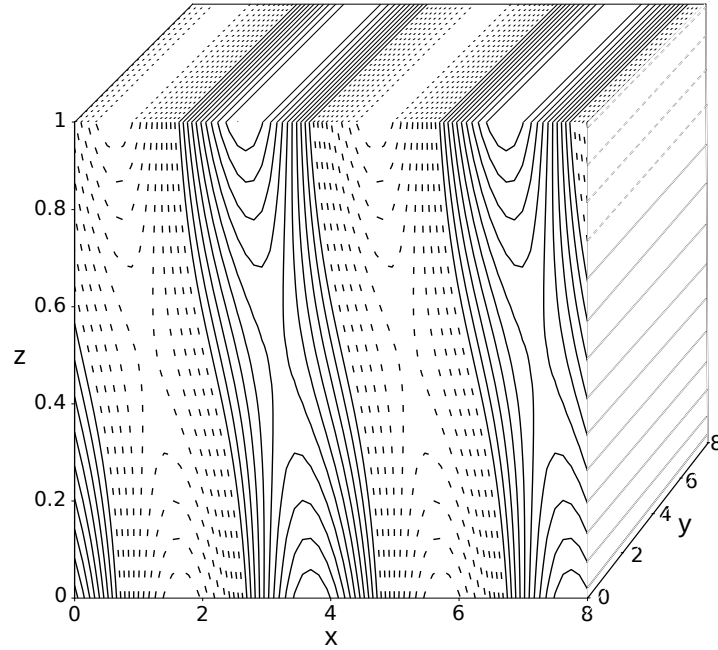


Figure 2: 3D representation of the Eady wave pattern. 20 days linear model run with an initial condition given by (25). x and y are non-dimensionalized using L_d and z with H

To validate the model, both the model's and the analytical growth rates for each zonal wavenumber (k_x) are obtained and compared, as shown in Figure 3. In the analytical case,

$$\sigma_E(k_x) = k_x \Im(c) \frac{L_d}{U_{\max}} \quad (28)$$

is used (Vallis, 2017), where $\Im(c)$ is the imaginary part of (26). For a clearer visualization of the growth rate, L_x is increased in Figure 3 up to 30000 km. Using (24) to obtain the maximum growth rate around the 8th wavenumber. To obtain the growth rate of the model, a simulation is run for each of the different wavenumbers using (25). The maximum v is computed at each time step, starting after the 80% of the simulation time had elapsed. This choice of a delay in the velocity calculation is justified by the trends observed in Figure 4 d), where the maximum velocity for the linear and nonlinear model begins to follow a clear trend after the 15th day.

The exponential growth formula

$$A(t) = A_0 e^{\sigma_e t} \quad (29)$$

is used to obtain the growth rate, where $A(t)$ represents a quantity that evolves over time. In this case, A is the maximum value of v . The growth rate can be determined by obtaining the slope of a linear regression of the natural logarithm of v against the time. As highlighted in Figure 3, the model and analytical growth rate match well, with a peak of 0.31 between the 7th and the 8th wavenumbers, as expected from (2). Disso-

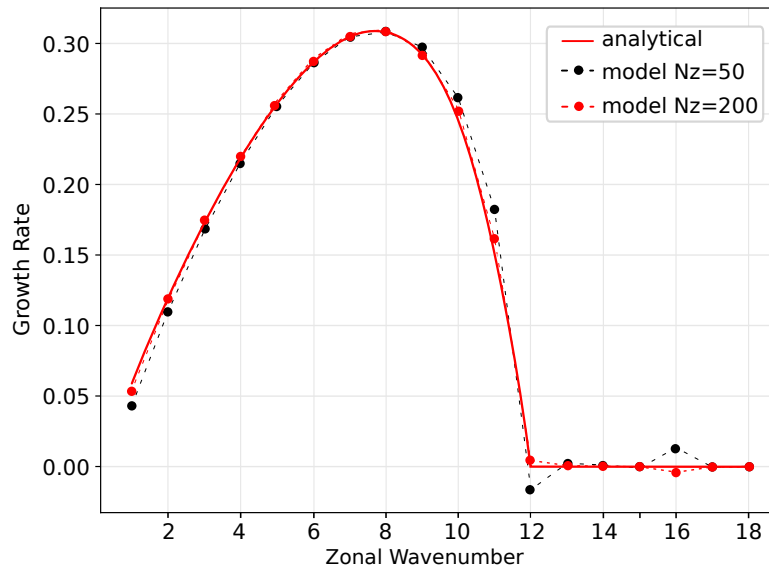


Figure 3: Growth rate vs zonal wavenumber. Normalized using L_d , (Vallis, 2017), with a peak of 0.31. $L_x = 30000$ km to have the maximum peak around the 8th wavenumber

nances observed at the 12th and 16th wavenumbers in the run with 50 vertical points are significantly reduced when the number of vertical points is increased, suggesting that these discrepancies are primarily related to the vertical resolution. This is likely due to the use of a finite difference scheme in the vertical direction, in contrast to the spectral scheme applied horizontally.

4.1 Linear vs nonlinear models

In the linear case, i.e. first part of Equation (17), contributions from $u'\partial q'/\partial x$ and from $v'\partial q'/\partial y$ will be lost. Figure 4 shows slightly lower values of v in the non-linear case than in the linear scenario. This can be perceived as a velocity dissipation in the nonlinear model due to a contribution of the nonlinear term $v'\partial q'/\partial y$, which is not present in the linear case. These linear-nonlinear differences are only presented when the initial perturbation is random and, thus, distributed between all the wavelengths. When (25) is used as an initial perturbation, the linear and nonlinear models have the same growth rate and the two curves in Figure 4 are identical.

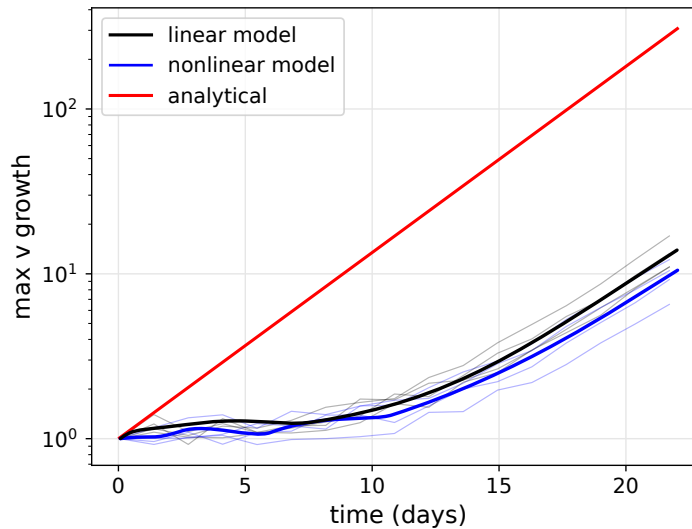


Figure 4: Maximum meridional velocity growth, normalized by initial values, over time for the analytical solution, linear model, and nonlinear model, averaged across four random initial perturbations.

4.2 Initial perturbation

This subsection analyses different initial perturbations and their effects on the simulations. The main difference between an initial perturbation, as (25), and a random one, affecting only the top and bottom layers, lies in their influence on the growth rate over time. Initial perturbations as (25) that "hits" only one of the wavenumbers will get the characteristic Eady wave pattern much faster than random initial perturbations, which are exciting all the wavenumbers at the same time resulting in slower or more irregular amplifications.

These differences are portrayed in Figure 5, where v contour lines are presented at

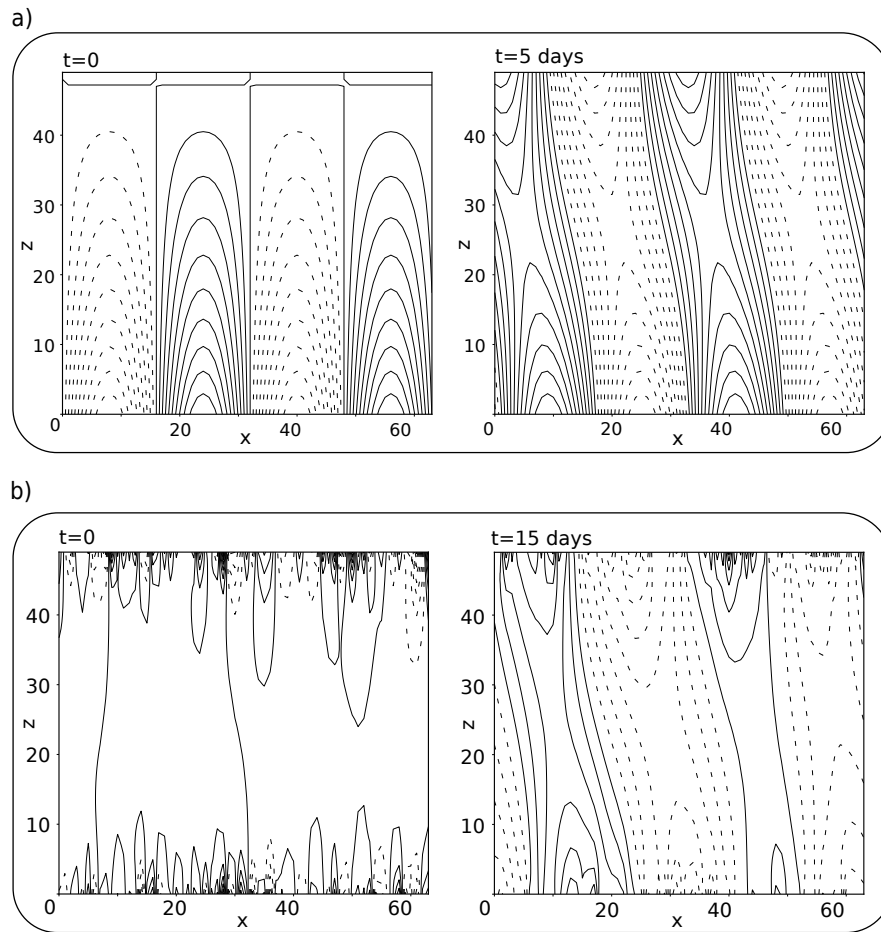


Figure 5: Contour lines for the meridional velocity at $L_y/2$, 20 contour lines between maximum and minimum. Dashed and solid lines for negative and positive values, respectively. **a)** Sinusoidal initial perturbation. Pattern given by (25) at $t = 0$. **b)** Random initial perturbation.

different time steps. Figure 5a) shows how after 5 days, an Eady wave pattern appears and it continues like that until the disturbance grows up to infinity. On the other hand, in Figure 5b), at $t = 0$ all the energy is condensed on the upper and lower boundaries. After 15 days, it is perceptible how the random state still has some effects on the boundaries. It stands that the maximum value of v is also affected by the initial perturbation, where the wavy initial condition exhibits lower velocities as if the perturbation is distributed through all of the wavenumbers.

4.3 Coriolis parameter

One parameter that plays a key role in how Eady waves emerge and evolve is the Coriolis parameter, f_0 . In this project, this parameter is set to 0.0001 rads^{-1} as default. In this subsection, it will remain constant, whereas, this value will be modified according to (27). β is also taken into account, something that most of the available works are neglecting due to the f-plane framework related to the Eady model. In this model, β is set equal to zero as default, although it can also be provided as a constant following (27).

The growth rate and the maximum value that the meridional velocity can reach is affected due to the Coriolis and β parameters. Figure 6 displays how these values change for different values of β and f_0 . The growth rate for the random initial perturbation in Figure 6a) shows different behaviors between the simulation with β and no- β effect, where in general, $\beta \neq 0$ presents a lower growth rate values. At mid-latitudes, the beta

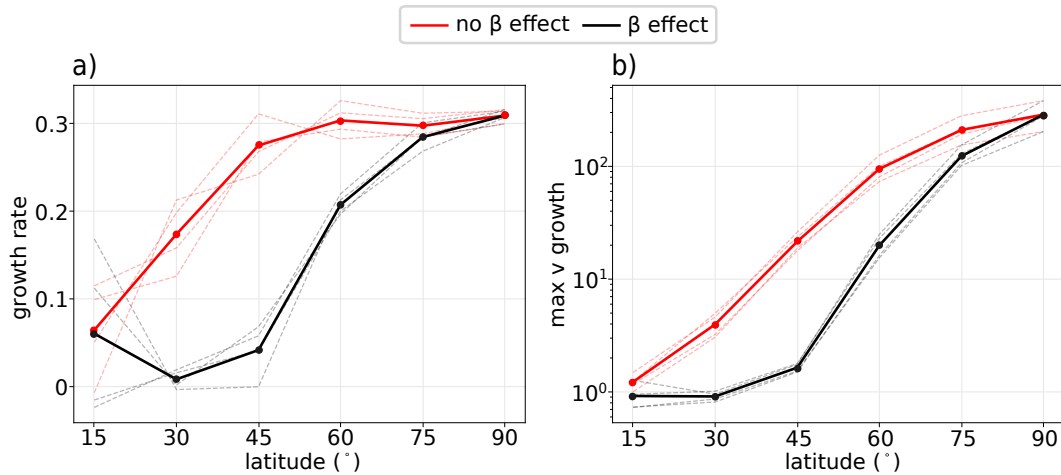


Figure 6: Mean of four simulations with different random perturbations. a) growth rate and b) maximum growth of v after 20 days for different values of f_0 and β in the nonlinear model.

effect has a stronger effect in weakening the growth rate. The β effect is more effective in stabilizing the baroclinic instability for low wavenumbers by dispersing energy through planetary Rossby waves. For higher latitudes, the growth rate is recovered due to the lack of the β effect. This dampening effect at mid-latitudes is also presented in Figure 6b), where the biggest discrepancies between the β and no- β scenario appears at 45° .

Before moving on to different velocity profiles, a summary of how the various parameters affect the growth rate and the maximum meridional velocity is shown in Table 1 and Figure 7. It is visible how the presence of β dissipate the maximum meridional velocity and thus, the growth rate. The highest growth is presented for the setups with no- β and constant density.

Although Figure 7 shows that the nonlinear and linear setups have similar behaviours, nonlinear simulations leads to an amplification of the growth rate around the 40th day. This amplification can result in the rapid growth of wave amplitudes, causing explosive increases. This is due to the nature of nonlinear simulations, where the energy tends to spread to smaller wavelengths. Due to the lack of dissipative effects, this energy start to accumulate in smaller wavelengths and ends up violating the CFL condition.

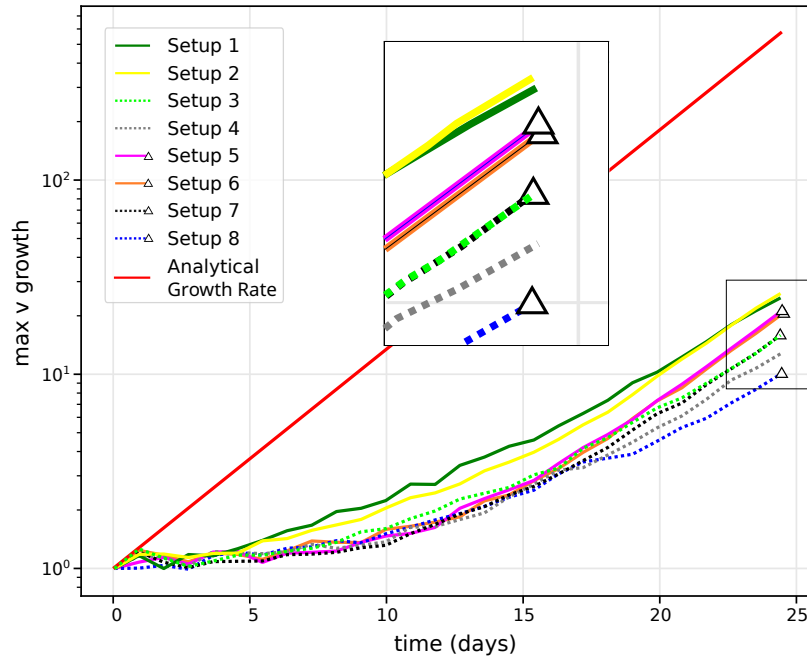


Figure 7: Maximum meridional velocity for the different setups in Table 1, where odd and even setup curves point out the linear and nonlinear cases, respectively, dotted and solid lines the β and non- β effects, and the triangles the cases where the density varies with height.

Setup	Growth rate	Model type	Beta effect	Density
1	0.267	Linear	False	ρ_0
2	0.260	Nonlinear	False	ρ_0
3	0.219	Linear	True	ρ_0
4	0.213	Nonlinear	True	ρ_0
5	0.247	Linear	False	$\rho(z)$
6	0.237	Nonlinear	False	$\rho(z)$
7	0.220	Linear	True	$\rho(z)$
8	0.195	Nonlinear	True	$\rho(z)$

Table 1: Growth rate for different combinations of model parameters after 30 days, obtained with the mean of three different random initial perturbations..

4.4 Modified velocity profiles

Before implementing different velocity profiles; U_{\max} value, as (28) states, affects the growth rate and, thus, the time needed for reaching the same instability. This is displayed in Figure 8, where the necessary time for reaching a meridional velocity perturbation 100 times bigger than the initial one increases exponentially with the decrement of U_{\max} . This is due to the energy conversion from the background flow to perturbations, where higher U_{\max} indicates more available energy.

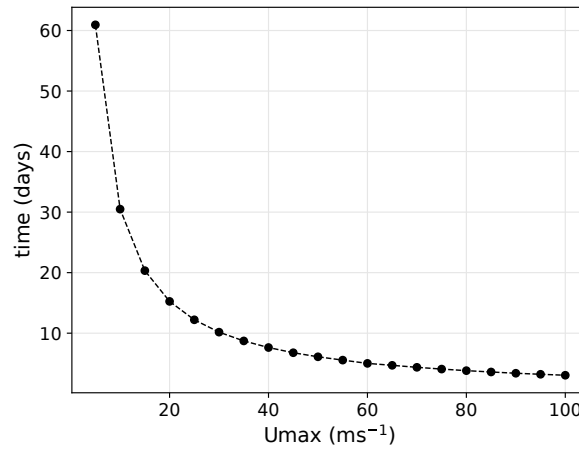


Figure 8: Time vs. maximum zonal velocity, with each point indicating when the simulation reaches 100 times the initial maximum meridional velocity, for random initial perturbations in the nonlinear and β setup.

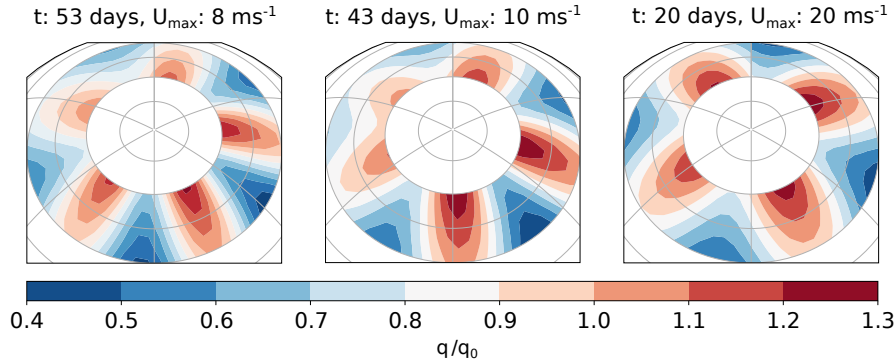


Figure 9: Projection of horizontal potential vorticity, normalized by q_0 , at $L_z/2$, centered at 60° N between 50° N and 70° N, for the corresponding domain size. Three simulations with different U_{\max} are shown, with simulations ending when the meridional velocity reaches 1000 times its initial value (nonlinear β model).

Figure 9 depicts how the pattern that emerges is also dependent on U_{\max} . A symmetric pattern of 5 maximal appears for U_{\max} around 8 ms^{-1} , and two of these maximal start to merge until a 4 maximal fully appears for U_{\max} around 20 ms^{-1} . This transition from 5 to 4 maximal illustrates the baroclinic instability dependency on the background flow, where stronger shear favours shorter wavelengths, causing neighbouring maxima to interact and combine. A similar scenario takes place in the real atmosphere, where stronger winds (e.g., during winter) leads to fewer and more intense Rossby waves (Riboldi et al., 2022).

Polynomial shear profiles

A family of polynomial shear profiles that follows the expression

$$U_0(z) = U_{\max} \left(\frac{z}{L_z} \right)^n, \quad (30)$$

has been studied using the present model.

These functions represent progressively steeper vertical shear layers, where the velocity increases as a higher-order polynomial with the vertical coordinate z , as depicted in Figure 10b), normalized by L_z . Figure 10a) shows how a relation between the higher order of the polynomials and the zonal wavenumber can be established, where higher polynomial order reaches their maximum growth rate for bigger zonal wavenumber. For small n , the shear is more distributed in the vertical domain which supports the growth

of instabilities in a wider range of zonal wavenumber, whereas, larger n 's concentrates the flow next to the upper boundary. These higher n profiles favour smaller scale instabilities due to stronger localized gradients.

Figure 10c) shows the maximum meridional velocity growth for a random initial perturbation. The maximum growth takes place around $n = 11$. After that, it starts to decrease again. The random initial perturbation ensures that the most unstable mode grows at its maximum rate.

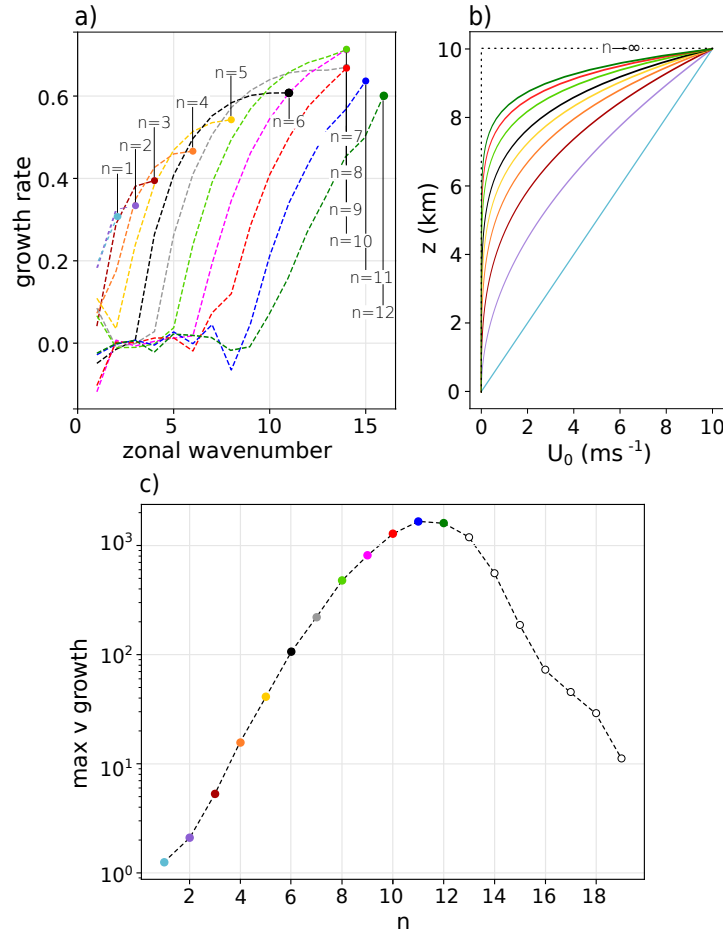


Figure 10: Linear simulations for each n in (30), with each velocity profile represented by a different color. **a)** Growth rate of wavy initial perturbations vs. zonal wavenumbers for each velocity profile over 20 days, with dots making the n of maximum growth. **b)** Velocity profile for each order. **c)** Maximum meridional velocity growth vs. n for random initial perturbations after 10 days.

Real case scenario

The "monthly averaged reanalysis" from 1940 to 2024 ERA5 data is acquired and processed to obtain a realistic vertical profile (Hersbach et al., 2023). Zonal and meridional velocities are averaged and taken between 50° N and 70° N. A representation of how the climatological mean of the velocity changes with height appears in Figure 11. The Eady model is a model with two vertical rigid lids, thus, the troposphere is a good region for testing it, where the bottom lid is the ground and the top lid is the tropopause.

A first-order curve

$$U = U_{\max} \left[0.94 \left(\frac{z}{L_z} \right) + 0.06 \right] \quad (31)$$

is fitted to the ERA5 velocity profile up to 10km. For the simulations with this vertical profile, the nonlinear model is used with a L_x set as 13000 km, which is approximately the circumference at 60° N. L_y is 2200 km, which corresponds with the distance between 50° and 70° N. U_{\max} is chosen as 12 ms^{-1} , which is the obtained mean of the maximum velocity at the troposphere. The model starts with a random initial perturbation to excite all wavenumbers. Additionally, the β -effect and $\rho(z)$ are considered to create a more realistic scenario.

Finally, figure 12 illustrates how q evolves with these conditions. The first figure shows the horizontal potential vorticity normalized by q_0 at the initial state. After 22 days,

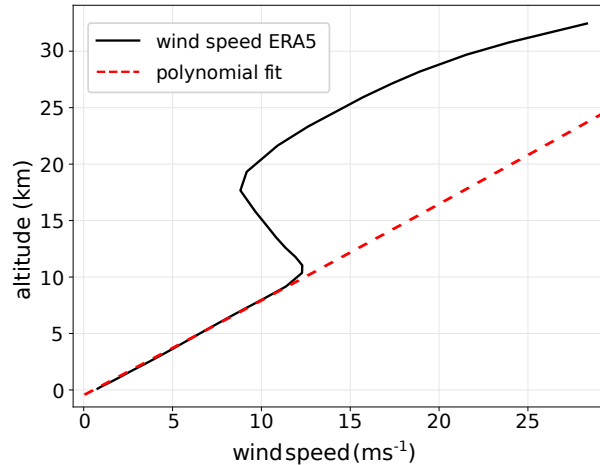


Figure 11: Climatological mean of the velocity profile around 50N-70N between 1940-2024, where the red dotted line represents the first order polynomial fit for the troposphere given by (31).

disturbances grow and the potential vorticity contours begin to distort. This reflects a growing baroclinic wave structure with troughs and ridges moving to the right. These curves appear due to the interaction of counter-propagating Rossby waves, as stated in Figure 1, modifying the horizontal potential vorticity field as energy is redistributed. Finally, after 30 days the shape is more pronounced forming a wave pattern and the potential vorticity values increase due to the transition toward nonlinear dynamics, having a rapid extraction of energy from the background flow.

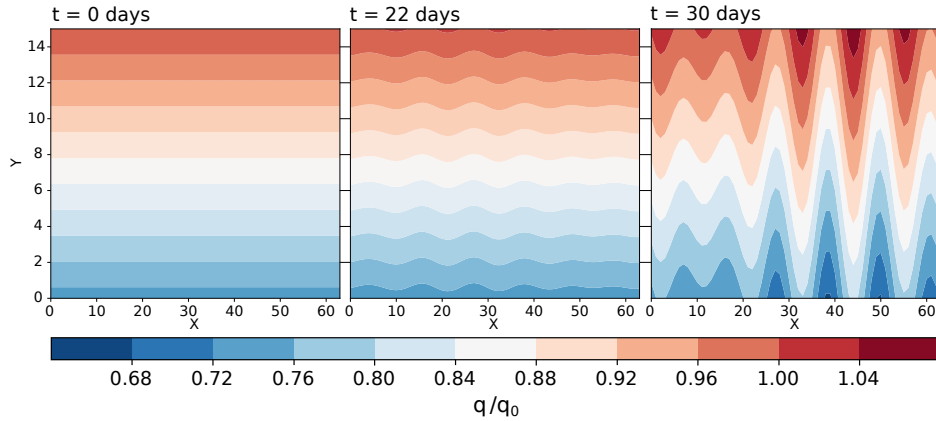


Figure 12: Evolution of horizontal potential vorticity at $L_z/2$ at the initial time, 22 days, and 30 days, respectively, under the conditions described in this subsection.

5 Conclusions

This work revisited the Eady problem, by analyzing both linear and nonlinear dynamics using a pseudospectral technique. The computational results were successfully validated against the analytical solution, establishing confidence in the numerical implementation. Through simulations using different initial perturbations, velocity profiles, and Coriolis parameter configurations, the project highlighted key aspects affecting wave growth rates and meridional velocities.

Key findings include the distinct dynamics of linear and nonlinear models, where nonlinear effects introduce velocity dissipation and are the driver of the intensification of the instability due to the interaction between the different wavenumber in later timesteps. The impact of the Coriolis parameter (f_0) and its variation with latitude (β -effect) was also explored, showcasing how these factors stabilize or amplify baroclinic instability. Modified velocity profiles demonstrated how sharper shear gradients favour shorter wavelength disturbances, intensifying instability, and having a growth rate strongly dependant on the maximum zonal wind value.

Finally, implementing a realistic vertical wind profile, using ERA5 reanalysis data, revealed patterns consistent with observed atmospheric phenomena.

5.1 Future work

This project serves as a foundation to explore more complex processes. The absence of a time-dependent shear profile causes baroclinic instabilities to grow indefinitely, as they are "fed" by the constant background flow. This prevents nonlinear effects from dispersing the accumulated energy. To achieve a variable background profile and obtain more realistic results, it would be necessary to remove periodicity in the y -axis. However, this would result in the loss of the Fourier spectral method's advantages in the y -direction.

A potential future development could involve migrating the simulations to a spherical domain, ensuring periodicity in both x and y coordinates. This approach would allow additional physical processes to emerge, such as frontogenesis, offering a more realistic scenario of the atmospheric dynamics.

References

- C. Bardos and E. Tadmor. Stability and spectral convergence of fourier method for nonlinear problems. on the shortcomings of the 2/3 de-aliasing method, 2013. URL <https://arxiv.org/abs/1308.5314>.
- R. Courant. Courant-friedrichs-lewy condition, 2018.
- E. T. Eady. Long waves and cyclone waves. *Tellus*, 1(3):33–52, 1949. doi: 10.3402/tellusa.v1i3.8507. URL <https://doi.org/10.3402/tellusa.v1i3.8507>.
- S. T. Garner, N. Nakamura, and I. M. Held. Nonlinear equilibration of two-dimensional eady waves: A new perspective. *Journal of Atmospheric Sciences*, 49(21):1984–1996, 1992. doi: 10.1175/1520-0469(1992)049<1984:NEOTDE>2.0.CO;2. URL https://journals.ametsoc.org/view/journals/atsc/49/21/1520-0469_1992_049_1984_neotde_2_0_co_2.xml.
- H. Hersbach, B. Bell, P. Berrisford, G. Biavati, A. Horányi, S.J. Muñoz, J. Nicolas, C. Peubey, R. Radu, I. Rozum, D. Schepers, A. Simmons, C. Soci, D. Dee, and J.N. Thépaut. Era5 monthly averaged data on single levels from 1940 to present, 2023. (Accessed on 19-11-2024).
- B. J. Hoskins, M. E. McIntyre, and A. W. Robertson. On the use and significance of isentropic potential vorticity maps. *Quarterly Journal of the Royal Meteorological Society*, 111(470):877–946, 1985. doi: <https://doi.org/10.1002/qj.49711147002>. URL <https://rmets.onlinelibrary.wiley.com/doi/abs/10.1002/qj.49711147002>.
- A. Iserles. Generalized leapfrog methods. *IMA Journal of Numerical Analysis*, 6(4):381–392, 10 1986. ISSN 0272-4979. doi: 10.1093/imanum/6.4.381. URL <https://doi.org/10.1093/imanum/6.4.381>.
- M. V. Kalashnik and O. Chkhetiani. An analytical approach to the determination of optimal perturbations in the eady model. *Journal of the Atmospheric Sciences*, 75(8):2741–2761, 2018. doi: 10.1175/JAS-D-18-0089.1. URL <https://journals.ametsoc.org/view/journals/atsc/75/8/jas-d-18-0089.1.xml>.
- M.V. Kalashnik, M.V. Kurgansky, and O.G. Chkhetiani. Baroclinic instability in geophysical fluid dynamics. *Phys.-Usp.*, 65:1039–1070, 2022.
- L. Lévesque. Revisiting the nyquist criterion and aliasing in data analysis. *European Journal of Physics*, 22(2):127, mar 2001. doi: 10.1088/0143-0807/22/2/304. URL <https://dx.doi.org/10.1088/0143-0807/22/2/304>.

- N. Mendes, M. Chhay, J. Berger, and D. Dutykh. *Spectral Methods*, page 167–209. Springer International Publishing, 2019. ISBN 9783030315740. doi: 10.1007/978-3-030-31574-0_8. URL http://dx.doi.org/10.1007/978-3-030-31574-0_8.
- H. Mukougawa and T. Ikeda. Optimal excitation of baroclinic waves in the eady model. *Journal of the Meteorological Society of Japan. Ser. II*, 72(4):499–513, 1994. doi: 10.2151/jmsj1965.72.4.499.
- R.T. Pierrehumbert and K.L. Swanson. Baroclinic instability. *Annual Review of Fluid Mechanics*, 27(Volume 27, 1995):419–467, 1995. ISSN 1545-4479. doi: <https://doi.org/10.1146/annurev.fl.27.010195.002223>. URL <https://www.annualreviews.org/content/journals/10.1146/annurev.fl.27.010195.002223>.
- J. Riboldi, E. Rousi, F. D’Andrea, G. Rivière, and F. Lott. Circumglobal rossby wave patterns during boreal winter highlighted by space–time spectral analysis. *Weather and Climate Dynamics*, 3(2):449–469, 2022. doi: 10.5194/wcd-3-449-2022. URL <https://wcd.copernicus.org/articles/3/449/2022/>.
- C. Shih-Nan, C. Chiou-Jiu, and J. A. Lerczak. On baroclinic instability over continental shelves: Testing the utility of eady-type models. *Journal of Physical Oceanography*, 50(1):3–33, 2020. doi: 10.1175/JPO-D-19-0175.1. URL <https://journals.ametsoc.org/view/journals/phoc/50/1/jpo-d-19-0175.1.xml>.
- G. K. Vallis. *Atmospheric and Oceanic Fluid Dynamics: Fundamentals and Large-Scale Circulation*. Cambridge University Press, 2 edition, 2017.
- R. T. Williams. Atmospheric frontogenesis: A numerical experiment. *Journal of Atmospheric Sciences*, 24(6):627–641, 1967. doi: 10.1175/1520-0469(1967)024<0627:AFANE>2.0.CO;2. URL https://journals.ametsoc.org/view/journals/atsc/24/6/1520-0469_1967_024_0627_afane_2_0_co_2.xml.